Self-Consistent Time-DomainLarge-Signal Model of High-Speed Traveling-Wave ElectroabsorptionModulators

Original
Self-Consistent Time-DomainLarge-Signal Model of High-Speed Traveling-Wave ElectroabsorptionModulators / Cappelluti, F., Ghione, G.. - In: IEEE TRANSACTIONS ON MICROWAVE THEORY AND TECHNIQUES. - ISSN 0018-9480. - 51:(2003), pp. 1096-1104. [10.1109/TMTT.2003.809672]

Publisher:
IEEE

Published
DOI:10.1109/TMTT.2003.809672

Self-Consistent Time-Domain Large-Signal Model of High-Speed Traveling-Wave Electroabsorption Modulators

Federica Cappelluti, *Member, IEEE,* and Giovanni Ghione, *Senior Member, IEEE*

***Abstract*—A new self-consistent large-signal model for traveling-wave electroabsorption modulators (TW EAMs) is presented. A time-domain finite-difference approach is exploited to carry out a fully coupled analysis of the nonlinear distributed interaction between the microwave and optical fields in the device. RF and optical nonlinearities and saturation effects are taken into account, as well as the influence on the microwave electrode propagation parameters of the nonuniform distribution of the optical power along the traveling direction. The model is applied to the analysis of a InGaAsP/InP TW EAM in small- and large-signal operation. Its performance in terms of bandwidth, linearity, and chirp are investigated as examples of application. The technique is validated in small-signal low optical-power condition through a comparison with the results of a small-signal frequency-domain approach.**

***Index Terms*—Electroabsorption modulators (EAMs), time-domain analysis, traveling-wave (TW) devices.**

I. INTRODUCTION

HIGH-SPEED high-efficiency electroabsorption modulators (EAMs) are key devices for the development of many optical communication systems including high-data-rate optical wavelength division multiplexing (WDM), high-speed optical time division multiplexing (OTDM), and microwave analog fiber optic links. By combining the optical and microwave propagation on the same guiding structure, the traveling-wave design allows to overcome the *RC* bandwidth limitation inherent to lumped devices, achieving high bandwidth and high modulation efficiency as well [1], [2].

In order to optimize the modulator performance, it is of primary interest to develop accurate microwave models of the device. In fact, the bandwidth limitation of EAMs largely derives from microwave losses in the transmission line and from asynchronous coupling to the optical signal, not to mention impedance mismatch issues, which are hard to manage in traveling-wave electroabsorption modulators (TW EAMs), whose characteristic impedance is significantly lower than 50 Ω. Moreover, in TW EAMs, several nonlinear effects take place, affecting the microwave and optical fields propagation, as well as their interaction. Firstly, the microwave transmission line (MTL) is nonlinear due to the voltage dependence of the junction capacitance, which is the main (albeit not the only) contribution to the overall line capacitance. The high optical absorption then generates a significant photocurrent, which, in turn, modifies the propagation characteristics of the line. In small-signal conditions, the small-signal per-unit-length (p.u.l.) photocurrent is a linear function of the local voltage, and can be conveniently described by a differential conductance model [3]. However, in large-signal conditions, the photocurrent nonlinearly depends on the local voltage (due to absorption saturation as a function of the applied voltage), but also exhibits saturation as a function of the optical power (due, e.g., to carrier screening effects, in much the same way as in high-power photodiodes). Finally, in EAMs, there is, at least in principle, a feedback between the optical and microwave line, in the sense that the line voltage modifies the optical waveguide absorption, but this, in turn, introduces a photocurrent that influences the microwave-line parameters; moreover, the microwave line is nonuniform since its parameters depend on the local optical power, which decreases along the line.

A first modeling approach, proposed in [3], concerns a quasi-static frequency-domain treatment of the TW EAM. The model assumes uniform bias and losses along the microwave line and exploits linearized relationships for the voltage-dependent optical absorption and the voltage-dependent photodetected current. Since the optical power is a component of the dc operating point, two different small-signal conditions and models arise for the ON/OFF states of the modulator, according to the level of optical power along the device. This model, proven to yield good agreement with experimental results [4], can capture the overall frequency response of the device and the effects of the optical power on the microwave propagation characteristics. However, as will be shown in Section III-A, some inaccuracies may arise under high optical power, when the nonuniformity of the bias voltage, as well as of the microwave-line parameters, are no longer negligible. Moreover, the aforementioned nonlinear effects cannot be included in linearized frequency-domain models. On the other hand, self-consistent dynamic large-signal modeling is essential in order to gain insight into microwave- and optical-power-induced saturation mechanisms to model harmonics and intermodulation products (IMPs) generation (analog applications), and to perform device design and optimization in large-signal operation (OTDM and WDM applications). In [5], some hints are given of a time-domain distributed model in which the nonlinear relationship between the voltage and complex refractive index is accounted for, while the microwave line is considered as linear; no back coupling exists

---

Manuscript received April 4, 2002; revised November 20, 2002. This work was supported in part by the Center of Excellence on Multimedia RadioCommunications (CERCOM), Politecnico di Torino under Project Line WP-2.

The authors are with the Dipartimento di Elettronica and CERCOM, Politecnico di Torino, I-10129 Turin, Italy (e-mail: federica.cappelluti@polito.it).

Digital Object Identifier 10.1109/TMTT.2003.809672

between the microwave and optical line, i.e., the microwave line works in low-power conditions, neglecting the effects of photocurrent and of nonuniform bias along the modulator. Time-domain approaches are commonly used in the modeling of electroabsorption modulated lasers (EALs) [6]–[8]. However, such modeling efforts are focused on the laser description, and leave in the background the modeling issue of the EAM portion of the device, usually treated as a lumped section, with voltage-dependent optical complex refractive index.

In this paper, we present a novel dynamic time-domain model of TW EAMs, featuring a fully coupled analysis of the nonlinear distributed interaction between the optical and microwave fields throughout the device. A circuit-oriented large-signal model is proposed for the microwave electrodes, treated as a nonlinear quasi-TEM transmission line with optical-power-dependent propagation characteristics. On the other hand, the optical field behavior in the device is studied by solving the wave equation taking into account the time/spatial variation of the optical complex refractive index, induced by the modulating microwave field. The overall device behavior is simulated by solving, through a finite-difference approach, the coupled equations describing the electrical and optical fields propagation along the device. Self-consistency is required since the absorbed optical power, locally dependent on the microwave field, drives the carriers generation, and the parameters of the electrical model are, in turn, photocurrent dependent. Both RF and optical-power saturation effects, including analog harmonic and IMP generation, can be simulated provided that proper models for the voltage dependence of the active region are inserted into the model. At the same time, chirp effects in the time domain are simulated together with the change of propagation characteristics with the incident optical power. The model can be extended so as to include in a self-consistent way other nonmodulating sections, such as a laser or a semiconductor optical amplifier (SOA).

This paper is organized as follows. Section II is devoted to the detailed description of the model equations and the numerical approach to the self-consistent simulation. Section III reports some simulation results in the small-signal, as well as large-signal operation. Finally, a brief conclusion is given in Section IV.

II. DISTRIBUTED TIME-DOMAIN MODEL

A. Microwave-Field Model

The electric equivalent circuit of a p.u.l. microwave electrode section is depicted in Fig. 1. In this circuit, L and C are the inductance and capacitance of the unloaded microwave electrode, while $Z_{\text{con}}(f)$ models the frequency-dependent (owing to skin effect) conductor impedance. The electroabsorption (EA) section is modeled through the device series resistance R_{S}, representing the resistivity of p- and n- semiconductor layers and metal contacts, the p-i-n junction capacitance $C_j\,(v_{\text{j}})$, the junction voltage-controlled dark current $i_{\text{D}}\,(v_{\text{j}})$, and the nonlinear photocurrent generator $I_{\text{ph}}\,(v_{\text{j}}, P_{\text{op}})$, which provides the coupling between the optical and MTLs. The quantities $v_{\text{j}}\,(z,t)$ and $P_{\text{op}}\,(z,t)$ are the junction voltage and optical power, respectively.

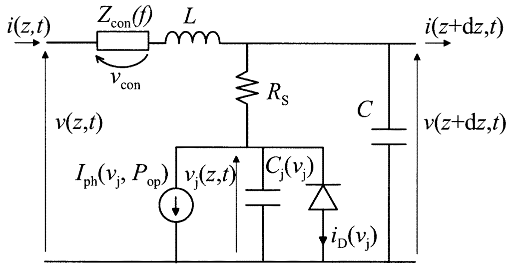

Fig. 1. Equivalent electric circuit for the p.u.l. MTL.

It is immediate to write the equations for the voltage and current in Fig. 1 as follows:

$$\frac{\partial v(z,t)}{\partial z} = -\,v_{\text{con}}\,(z,t) - L\frac{\partial i\,(z,t)}{\partial t} \tag{1}$$

$$\frac{\partial i\,(z,t)}{\partial z} = -\,\frac{v\,(z,t) - v_j\,(z,t)}{R_S} - C\frac{\partial v\,(z,t)}{\partial t}. \tag{2}$$

The junction voltage $v_{\text{j}}\,(z,t)$ and the total microwave voltage $v\,(z,t)$ are locally related through the following nonlinear dynamic equation:

$$v_{\text{j}}\,(z,t) = v\,(z,t) - R_{\text{S}}\left[C_j\frac{\partial v_{\text{j}}\,(z,t)}{\partial t} + I_{\text{ph}}\big(v_j\,(z,t)\,, P_{\text{op}}\,(z,t)\big) + i_{\text{D}}\right] \tag{3}$$

where, for the sake of brevity, we have omitted the dependence on v_{j} of C_{j} and i_{D}. The second term on the right-hand side of (3) is the voltage drop across the p-i-n junction resistance R_{S}. The voltage drop across the frequency-dependent impedance $Z_{\text{con}}(f)$ can be computed in the time-domain through a convolution such as

$$v_{\text{con}}\,(z,t) = z_{\text{con}}\,(t) * i\,(z,t) \tag{4}$$

where $z_{\text{con}}\,(t)$ denotes the inverse Fourier transform of $Z_{\text{con}}(f)$. The numerical solution of (4) can be accomplished through a discrete-time recursive formula (as will be discussed in Section II-C).

The MTL equations (1), (2) can be conveniently reformulated in a forward–backward traveling-wave approach. To this aim, we introduce the following nonsingular linear variable transformations:

$$v_{\text{F}}\,(z,t) = \frac{1}{2}\big[v\,(z,t) - Z_0 i\,(z,t)\big] \tag{5}$$

$$v_{\text{R}}\,(z,t) = \frac{1}{2}\big[v\,(z,t) + Z_0 i\,(z,t)\big] \tag{6}$$

where $Z_0 = \sqrt{L/C}$ is the characteristic impedance associated to the ideal transmission line (L, C). By substituting (5) and (6) in the MTL equations (1), (2), after some algebra, we obtain the traveling-wave formulation

$$\frac{\partial v_{\text{F}}\,(z,t)}{\partial z} + \frac{1}{v_f}\frac{\partial v_{\text{F}}\,(z,t)}{\partial t} = -K_1\big[v_{\text{F}}\,(z,t) + v_{\text{R}}\,(z,t) - v_{\text{j}}\,(z,t)\big] - K_2 v_{\text{con}}\,(z,t) \tag{7}$$

$$\frac{\partial v_{\mathrm{R}}(z,t)}{\partial z} - \frac{1}{v_f}\frac{\partial v_{\mathrm{R}}(z,t)}{\partial t} = K_1\big[v_{\mathrm{F}}(z,t) + v_{\mathrm{R}}(z,t) - v_{\mathrm{j}}(z,t)\big] - K_2 v_{\mathrm{con}}(z,t) \tag{8}$$

where $K_1 = Z_0/2R_{\mathrm{S}}$, $K_2 = 1/2$, and $v_f = 1/\sqrt{\mathrm{LC}}$. Finally, concerning the junction voltage v_{j}, by substituting (5) and (6) in (3), we have

$$\begin{aligned} v_j(z,t) =& v_F(z,t) + v_R(z,t) \\ &- R_S\left[C_j\frac{\partial v_j(z,t)}{\partial t} + I_{\mathrm{ph}}\big(v_j(z,t), P_{\mathrm{op}}(z,t)\big) \right. \\ &\left. + i_D\right]. \end{aligned} \tag{9}$$

Note that the simultaneous equations (7)–(9) are exactly equivalent to (1)–(3) since no approximation has been introduced. Thus, the voltages v_{F}, v_{R}, solutions of (7)–(9) may be used to derive the MTL voltage and current satisfying (1)–(3) by the relationships (5) and (6). In the following, for convenience, we will refer to the variables v_{F} and v_{R} as the forward and backward voltages on the line, respectively; however, the interpretation of v_{F} and v_{R} as such strictly holds only when the transmission line in Fig. 1 reduces to an ideal transmission line.

B. *Optical-Field Model*

We limit our analysis to a single-mode field propagating in the optical waveguide, the extension to the multimode case being straightforward. Moreover, we assume no reflections at the end facet of the modulator. This is a reasonable approximation as long as we study discrete EAMs since antireflection coatings are usually deposited on the facets of the device, and it can be expected that the residual reflections do not significantly influence the behavior of the modulator. However, if the model were extended to the analysis of an integrated laser-EAM structure, the approximation would no longer be acceptable. In fact, since the power reflected from the modulator section into the laser cavity changes with intensity modulation, it turns out to change the laser wavelength, i.e., it introduces chirp [9], [10].

The optical field in the EAM waveguide can be written as

$$E(x,y,z,t) = \phi(x,y)\, E_{\mathrm{F}}(z,t)\, e^{i\omega_{\mathrm{o}}t - i\beta_{\mathrm{o}}z} \tag{10}$$

where $\phi(x,y)$ is the modal function in the waveguide, the complex amplitude $E_{\mathrm{F}}(z,t)$ represents the forward slowly varying component of the optical field, ω_{o} is the laser optical frequency, and β_{o} is the unperturbed (i.e., in the absence of applied voltage) propagation constant. The amplitude $E_{\mathrm{F}}(z,t)$ can be derived from Maxwell's equations by exploiting the slowly varying envelope approximation and treating the electric-field induced variations of the optical complex refractive index as a small perturbation [11]. The time-dependent traveling-wave equation describing the optical field propagation results as follows:

$$\frac{1}{v_{\mathrm{go}}}\frac{\partial E_{\mathrm{F}}(z,t)}{\partial t} + \frac{\partial E_{\mathrm{F}}(z,t)}{\partial z} = \left[-\frac{\Delta\alpha(z,t)}{2} - \mathrm{i}\frac{\omega_o}{c}\Delta n_o(z,t)\right] E_{\mathrm{F}}(z,t) \tag{11}$$

where v_{go} is the optical group velocity, assumed to be constant over the frequency range of interest, and c is the speed of light in vacuum; $\Delta\alpha(z,t)$ and $\Delta n_{\mathrm{o}}(z,t)$ may be written as

$$\Delta\alpha(z,t) = \Gamma_{\mathrm{o}}\Delta\alpha_{\mathrm{m}}\big(V_j(z,t), P_{\mathrm{op}}(z,t)\big) \tag{12}$$

$$\Delta n_{\mathrm{o}}(z,t) = \Gamma_{\mathrm{o}}\Delta n_{\mathrm{m}}\big(V_j(z,t), P_{\mathrm{op}}(z,t)\big) \tag{13}$$

where Γ_{o} is the optical confinement factor in the active layer and $\Delta\alpha_{\mathrm{m}}$ and Δn_{m} are the voltage/power-dependent changes of the optical absorption coefficient and refractive index in the active layer, respectively. Analytical models for $\Delta\alpha_{\mathrm{m}}$ and Δn_{m} can be derived by curve fitting either from experimental data or from physics-based simulations of the active region structure. Finally, the optical propagation constant in (10) is given by

$$\beta_{\mathrm{o}} = \frac{\omega_{\mathrm{o}}}{c}n_{\mathrm{eff}} + \frac{\mathrm{i}}{2}(\alpha_{\mathrm{o}} + \alpha_{\mathrm{loss}}) \tag{14}$$

n_{eff} and α_0 being the effective refractive index and optical-power EA coefficient at transparency (i.e., $V = 0$). The term α_{loss} accounts for all those mechanisms, such as free-carrier absorption and scattering loss, which cause optical attenuation without generation of carriers. To complete our model, we write the p.u.l. photocurrent I_{ph} as

$$I_{\mathrm{ph}}(z,t) = \frac{q}{\hbar\omega_{\mathrm{o}}}\alpha(z,t)P_{\mathrm{op}}(z,t) \tag{15}$$

where q is the electric charge, $\hbar$ is the rationalized Planck's constant, $\alpha(z,t)$ is given as $\alpha = \alpha_0 + \Delta\alpha$, and P_{op} is the optical power

$$P_{\mathrm{op}}(z,t) = |E(x,y,z,t)|^2 = |E_{\mathrm{F}}(z,t)|^2 e^{-(\alpha_0 + \alpha_{\mathrm{loss}})z}. \tag{16}$$

The previous equations stress the aforementioned interplay between the microwave and optical traveling fields as follows:

- optical-power dependence of I_{ph} (15), which affects the propagation characteristics of the MTL and, thus, the effective modulating voltage along the device through (7)–(9);
- junction voltage dependence of the optical absorption (and refractive index) which, in turn, affects the optical field propagation and the photogenerated current according to (11) and (15), respectively.

Indeed, a fully coupled solution is required in order to correctly describe such nonlinear distributed interaction.

The small-signal equivalent circuit adopted in [3] can be derived from the one proposed in Fig. 1 by approximating the p.u.l. photocurrent generator $I_{\mathrm{ph}}(z,t)$ as an optical-power-dependent resistor $R_0 = (dI_{\mathrm{ph}}/dv_j)^{-1}$ evaluated at the junction bias voltage $V_{\mathrm{j}} = V_{\mathrm{b}}$. In fact, since the photocurrent generator depends on $v_{\mathrm{j}} = V_{\mathrm{b}} + v(t)$, one has

$$I_{\mathrm{ph}} = f(v_{\mathrm{j}}) \approx f(V_{\mathrm{b}}) + \left.\frac{df}{dv_j}\right|_{V_{\mathrm{b}}} v(t) + \cdots$$

where the second (linear) term simply is a conductance. The linear approach in [3] assumes the whole length of the device to operate at the same bias point; this, in turn, implies the dc

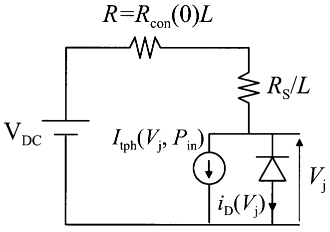

Fig. 2. Lumped equivalent circuit of the TW EAM in dc operation.

optical absorption $\alpha_{\mathrm{b}} = \alpha(V_b)$ to be z-independent. Following this approach, in dc operation, (2), (3), and (15) reduce to

$$\frac{dI}{dz} = -I_{\mathrm{ph}}(z) = -\frac{q}{\hbar\omega_o}\alpha_{\mathrm{b}}P_{\mathrm{op}}(0)e^{-(\alpha_{\mathrm{b}}+\alpha_{\mathrm{loss}})z}. \tag{17}$$

Integrating the previous equation, one has $I(L)-I(0) = -I_{\mathrm{tph}}$, where I_{tph} is the total photocurrent generated in the modulator

$$\begin{aligned} I_{\mathrm{tph}} &= \int_0^L I_{\mathrm{ph}}dz \\ &= \frac{qP_{\mathrm{op}}(0)}{\hbar\omega_o}\frac{\alpha_{\mathrm{b}}}{\alpha_{\mathrm{b}}+\alpha_{\mathrm{loss}}}\left(1-e^{-\alpha_{\mathrm{b}}L}e^{-\alpha_{\mathrm{loss}}L}\right) \end{aligned} \tag{18}$$

which is equivalent to the photodiode response. Note that, for the transmission line to be uniform, the total photocurrent is equally spread over the whole length of the line, i.e., $I_{\mathrm{ph}} = I_{\mathrm{tph}}/L$; the corresponding ac p.u.l. equivalent resistance, modeling the linearized dependence of I_{ph} on the junction voltage v_{j}, is

$$R_0 = \left(\frac{1}{L}\left.\frac{dI_{\mathrm{tph}}}{dv_{\mathrm{j}}}\right|_{V_{\mathrm{b}}}\right)^{-1}. \tag{19}$$

In order to evaluate R_0, we need to estimate the junction bias point $V_{\mathrm{j}} = V_{\mathrm{b}}$. To this aim, the EAM can be treated as equivalent to the lumped electric circuit shown in Fig. 2, where $R_{\mathrm{con}}(0)$ is the dc component of the conductor impedance and $I_{\mathrm{tph}}(V_{\mathrm{j}}, P_{\mathrm{in}})$ is given by (18), being $P_{\mathrm{in}} = P_{\mathrm{op}}(0)$, the incident optical power. Thus, the bias point satisfies the following nonlinear equation:

$$V_{\mathrm{j}} = V_{\mathrm{DC}} - R\left[I_{\mathrm{tph}}(V_{\mathrm{j}}, P_{\mathrm{in}}) + i_D(V_{\mathrm{j}})\right] \tag{20}$$

being $R = R_{\mathrm{con}}(0)L + R_{\mathrm{S}}/L$. Note that either the modulator bias point or the ac equivalent resistance R_0 depend on the optical power and absorption through (18); thus, different small-signal operating conditions arise depending on the optical power absorbed along the device. The consequence of the *uniform bias point* assumption exploited in [3] on the predicted performance of the TW EAM will be discussed in detail in Section III.

C. Numerical Algorithm

The numerical solution of the microwave and optical traveling-wave equations is obtained by a finite-difference approach [9]. The basic idea is to longitudinally divide the device into an integer number of small sections having equal length. Across each section, the propagation characteristics of the optical and microwave waveguides are assumed to be constant, but they are allowed to change from section to section. To account for the velocity mismatch between the optical and electrical signals, two different spatial grids must be used for the optical and microwave waveguides. The finite-difference approach is schematically illustrated in Fig. 3.

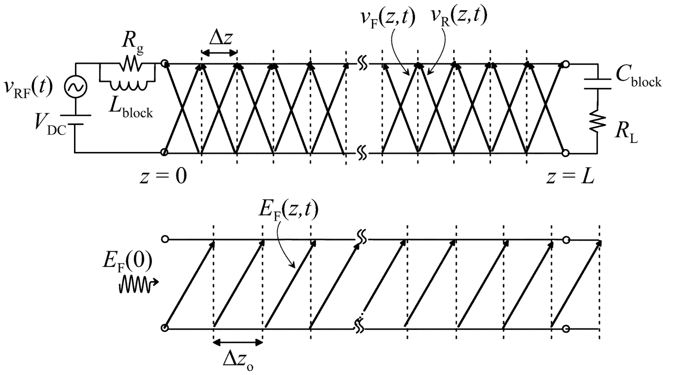

Fig. 3. Schematic view of the (*top*) microwave and (*bottom*) optical waveguides having an integer number of subsections of length Δz and Δz_o, respectively.

The time-dependent coupled MTL (7), (8) can be solved in the time domain by a first-order difference approximation of the partial differentials [9] yielding

$$\begin{aligned} v_{\mathrm{F}}(z+\Delta z, t+\Delta t) = &(1-K_1\Delta z)\, v_{\mathrm{F}}(z,t) - K_1\Delta z v_{\mathrm{R}}(z,t) \\ &+ K_1\Delta z v_{\mathrm{j}}(z,t) - K_2\Delta z v_{\mathrm{con}}(z,t) \end{aligned} \tag{21}$$

$$\begin{aligned} v_{\mathrm{R}}(z-\Delta z, t+\Delta t) = &-K_1\Delta z v_{\mathrm{F}}(z,t) + (1-K_1\Delta z)\, v_{\mathrm{R}}(z,t) \\ &+ K_1\Delta z v_{\mathrm{j}}(z,t) + K_2\Delta z v_{\mathrm{con}}(z,t) \end{aligned} \tag{22}$$

where we have set $\Delta z = v_f\Delta t$ and we have neglected the second derivatives terms. Since v_f does not include the effect of the junction capacitance, the choice of Δz is conservative with respect to the numerical stability of the finite-difference algorithm [12]. The solution of (9), locally relating the junction voltage v_{j} to the total voltage $v_{\mathrm{F}} + v_{\mathrm{R}}$ across the transmission line, has been achieved through a semi-implicit Euler method. The spatial discretization step Δz should be chosen small enough to ensure an accurate solution of the total voltages and currents along the microwave line. Specifically, Δz must be chosen small enough to make negligible the effect of the second-order derivatives omitted in (21) and (22), and to guarantee a rapid convergence in the integration of (9), i.e., $\Delta t = \Delta z/v_f \ll R_{\mathrm{S}}C_{\mathrm{j}}$. In this analysis the device length L is smaller or comparable to the guided wavelength and, therefore, the choice of Δz is not overly critical. In the simulations we have used Δz ranging from $L/100$ to $L/40$.

System (21) and (22) must be completed with the initial and boundary conditions for the forward and backward voltages at the beginning and end of the modulator. Initial conditions are imposed according to the applied bias. The capacitor C_{block} at the load section can be exploited to decouple the dc-bias generator from the load resistor. In a similar way, the inductor L_{block} at the input section decouples the dc bias from the RF generator resistor R_{g}. Thus, the boundary conditions for the bias can be written as

$$V_{\mathrm{F}}(0) = -V_{\mathrm{R}}(0) + V_{\mathrm{DC}} \tag{23}$$

$$V_{\mathrm{R}}(L) = V_{\mathrm{F}}(L) \tag{24}$$

where we have denoted with V_{F} and V_{R} the dc components of the forward and backward propagating waves. From the RF signal standpoint, the inductor and capacitor act as an open and short circuit, respectively, and the corresponding boundary conditions are

$$v_{\mathrm{F}}(0,t) = v_{\mathrm{R}}(0,t)\frac{R_{\mathrm{g}} - Z_0}{R_{\mathrm{g}} + Z_0} + \frac{Z_0}{R_{\mathrm{g}} + Z_0} e_{\mathrm{g}}(t) \tag{25}$$

$$v_{\mathrm{R}}(L,t) = \frac{R_L - Z_0}{R_L + Z_0} v_{\mathrm{F}}(L,t). \tag{26}$$

Finally, (4) has been numerically implemented through an infinite impulse response (IIR) digital filter. The frequency behavior of Z_{con}, known from experiments or physics-based simulations, is fitted with a rational function in the analog complex variable $s = i\omega$, and successively transformed in the digital z-transform domain by exploiting the bilinear transformation technique [13]. The resulting discrete-time simulator for the voltage drop $v_{\mathrm{con}}(\bar{t}, z)$ results as

$$v_{\mathrm{con}}(\bar{t}, z) = \sum_{j=0}^{P} c_j i(\bar{t} - j\Delta t, z) - \sum_{k=1}^{Q} d_k v_{\mathrm{con}}(\bar{t} - k\Delta t, z) \tag{27}$$

where c_j and d_k are the coefficients of the digital rational function approximating Z_{con}. Good accuracy is achieved provided that the time step is small enough so that $\Delta t \ll 1/2f_{\mathrm{max}}$, where f_{max} is the maximum frequency of interest.

Concerning the optical field propagation, by choosing $\Delta z_o = v_{\mathrm{go}}\Delta t$, the solution of (11) is given by [14]

$$\begin{aligned} &E_{\mathrm{F}}(z + \Delta z_{\mathrm{o}}, t + \Delta t) \\ &= \exp\left[\left(-\frac{\Delta\alpha(z,t)}{2} - \mathrm{i}\Delta\beta_{\mathrm{o}}(z,t)\right)\Delta z_{\mathrm{o}}\right] E_{\mathrm{F}}(z,t). \end{aligned} \tag{28}$$

Initial conditions are set according to the incident optical field.

The previous equations, coupled through (9), (12), (13), (15), and (16), are solved through a time-stepped iterative approach. For each time step, the optical and microwave fields will cover different spatial steps $\Delta z_{\mathrm{o}} = v_{\mathrm{go}}\Delta t$ and $\Delta z = v_f \Delta t$, respectively. To account for this asynchronous spatial propagation, which is a consequence of the velocity mismatch, a linear interpolation is exploited to switch from the optical to the microwave grid and *vice versa*. As a last remark, if the time step is chosen in order to divide the device length into an integer number of Δz sections, the resulting number of sections on the optical grid $(L/\Delta z_{\mathrm{o}})$ will not be an integer since usually v_f and v_{go} are incommensurate quantities. To overcome this, the simulated optical length is allowed to be larger than L, as shown in Fig. 3, and the value of the optical quantities at $z = L$ is recovered through a linear interpolation.

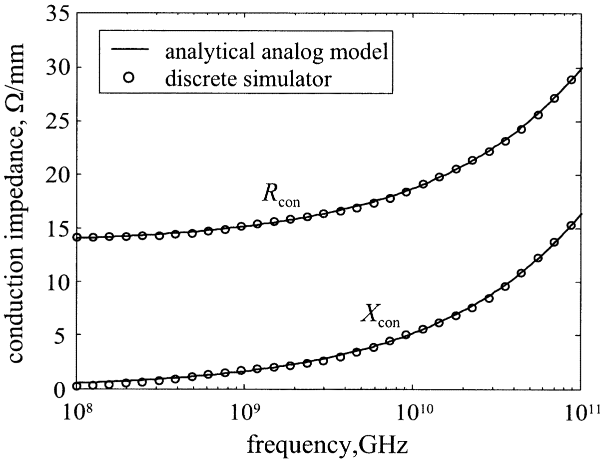

Fig. 4. Frequency behavior of the resistive (R_{con}) and inductive (X_{con}) components of the conduction impedance. Solid line (—): frequency-domain model, circles (o): time-domain simulation.

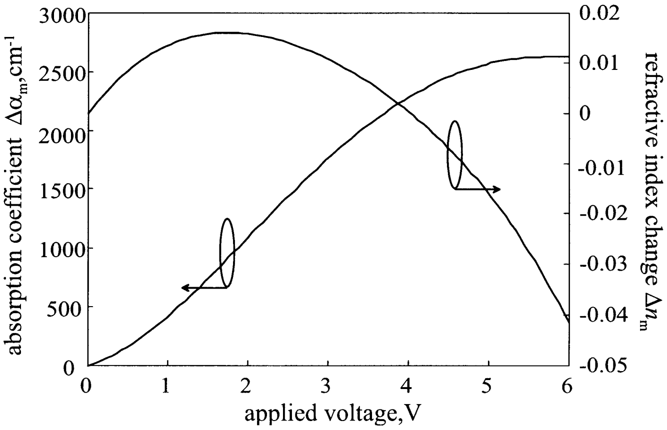

Fig. 5. Changes of the absorption and refractive index with bias voltage.

III. SIMULATION RESULTS

We have applied the model developed in Section II to study a standard multiple quantum well (MQW) InGaAsP/InP EAM, with a 3-μm–wide waveguide, 0.3-μm active layer thickness, and 200-μm length. The values assumed for the MTL equivalent-circuit parameters are (see, e.g., [3]) $L = 0.5$ nH/mm, $C = 0.4$ pF/mm, and $R_{\mathrm{S}} = 1$ Ωmm, and for the depleted p-i-n junction, $C_{\mathrm{j}} = 1.2$ pF/mm. For typical EAM devices, the dc leakage resistance $R_{\mathrm{j}} = v_{\mathrm{j}}/i_{\mathrm{D}}(v_j)$, as well as the ac leakage resistance $R_{\mathrm{jAC}} = dv_{\mathrm{j}}/di_{\mathrm{D}}$, take values around 10 kΩ or larger and, thus, they result to be negligible in static and small-signal operation, respectively. Moreover, R_{j} is usually weakly dependent on the junction voltage v_{j} [15], unless v_{j} approaches the p-i-n diode threshold voltage, i.e., under highly nonlinear operation. Thus, in the following analysis, we neglect the nonlinearity of R_{j}, as well as C_{j}, and focus on the optical mechanisms related nonlinearities. Finally, as for the conductor impedance, we assume a frequency behavior such as $Z_{\mathrm{con}}(f) = R + (1+\mathrm{i})R\sqrt{f/4f_0}$, with $R \sim 13.5$ Ω/mm and $f_0 \sim 17$ GHz. A seventh-order rational polynomial has been used to fit $Z_{\mathrm{con}}(f)$. Fig. 4 compares the analytical frequency behavior of $Z_{\mathrm{con}}(f)$ to the frequency behavior predicted by the discrete-time simulator in (27). The time step used was approximately 0.05 ps.

As for the optical parameters of the active layer, which is the change of absorption coefficient and refractive index with applied bias, we have used experimental data reported in [9]. Fourth-order polynomial functions have been used to fit $\Delta\alpha_{\mathrm{m}}$ and Δn_{m} between 0 and 6 V, at the operating wavelength of 1.544 μm. The behavior of $\Delta\alpha_{\mathrm{m}}$ and Δn_{m} as functions of the reverse applied bias is shown in Fig. 5. The optical confinement factor in the active layer is assumed to be $\Gamma_{\mathrm{o}} = 0.2$, while the residual absorption α_0 has been set to 15 dB/mm, which is a typical value for EAMs. An optical group index of 3.5 has been used. The overall contribution of free-carrier and scattering loss $(\alpha_{\rm loss})$ is usually limited to a few decibels per millimeter (see, e.g., [16] and [17]) and has been neglected in the following simulations.

Concerning the optical-power-induced saturation of the absorption coefficient, as well as of the refractive index change, we have used an empirical model based on experimental observations reported in the literature [18]. Measurements of the modulator photocurrent as a function of the incident optical power show that, after an initial linear growth with the optical power, as predicted from the theory (15), by further increasing the optical power, the photocurrent starts to saturate. To model this effect, we use a corrective optical-power-dependent factor, and compute the absorption coefficient as

$$\alpha(V, P_{\rm op}) = \alpha_{\rm m}(V) f_{\rm sat}(P) = \alpha_{\rm m}(V)\left(1 + \frac{P_{\rm op}}{P_{\rm op,th}}\right)^{-1}. \tag{29}$$

When $P_{\rm op} \gg P_{\rm op,th}$ we have $\alpha \approx \alpha_{\rm m} P_{\rm op,th}/P_{\rm op}$, i.e., the photocurrent density in (15) saturates. The empirical parameter $P_{\rm op,th}$ sets the value of incident optical power corresponding to half-absorption with respect to the zero optical-power condition; note that if $\alpha/L \gg 1$, this corresponds also to the half-detected photocurrent. From a practical standpoint, the level of optical power at which the photocurrent deviates from the linear behavior is strongly dependent on the structure of the active layer and on the electroabsorptive mechanism exploited. Obviously, more accurate models could be extracted from device measurements or physics-based simulations. In the following, we have assumed $P_{\rm op,th} = 50$ mW.

The resulting TW EAM static optical transmission has 3-dB residual loss at zero bias and contrast ratios of 10 and 20 dB at 1.3 and 2.1 V, respectively. In all the following simulations, the RF generator impedance is set to 50 Ω and the modulator is terminated on a resistor $R_{\rm L} = 35\ \Omega$, which corresponds to the ideal line impedance $Z_0 = \sqrt{L/C}$. The bias voltage generator is decoupled from both $R_{\rm g}$ and $R_{\rm L}$.

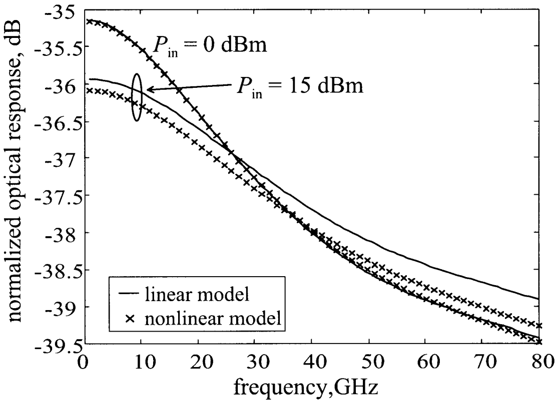

Fig. 6. Small-signal optical response, at different incident optical power, predicted by the linear (—) and nonlinear (x) models. The optical response is normalized to the input optical power.

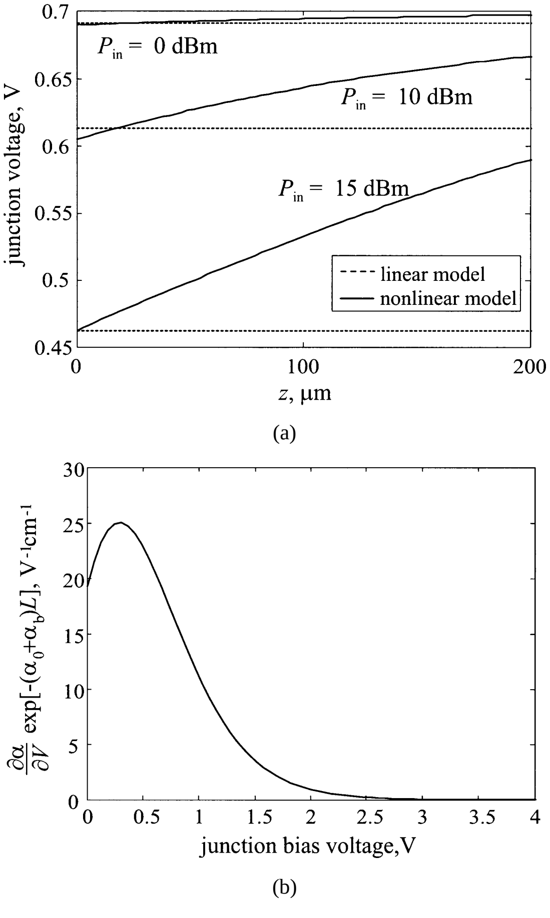

(a)

(b)

Fig. 7. (a) Junction voltage variation along the device, at different incident optical power, predicted by the nonlinear (solid lines) and linear (dashed lines) models. (b) Bias-dependent term of the ac optical response computed according to the linear model.

A. Small-Signal Analysis: Frequency Response

To validate our nonlinear model, in small-signal conditions, we have simulated the device under low optical illumination $(P_{\rm op} = 0$ dBm) and compared the results with the predictions of the linear model proposed in [3]. Fig. 6 shows the small-signal optical response, i.e., the peak-to-peak amplitude of the RF component of modulated optical power normalized to the incident optical power as a function of the RF signal frequency. The dc voltage source supplied 0.7-V bias and the amplitude of the RF signal was 1 mV. At low optical power $(P_{\rm op} = 0$ dBm), the linear and nonlinear models show an excellent agreement. At higher optical power, the low-frequency optical response drops, while the bandwidth increases. This is due to the larger photocurrent-induced microwave losses, which flatten the frequency response and increase the bandwidth (defined as the frequency at which the optical response drops by 3 dB with respect to the low-frequency limit). The effect is qualitatively captured by both models. However, the linear model results to be less accurate since it cannot account for the nonuniform microwave losses and the nonuniform EAM bias voltage that occur at higher optical power, as can be seen in Fig. 7(a), which depicts the variation of the junction voltage along the microwave line. At optical power of 15 dBm, the linear model significantly underestimates the junction voltage.

As reported in [3], the modulator small-signal response depends on the bias point through the term $\partial\alpha/\partial V_{\rm j} \exp[-(\alpha_0 + \alpha(V_{\rm j}))L]$. This term is plotted in Fig. 7(b) as a function of the

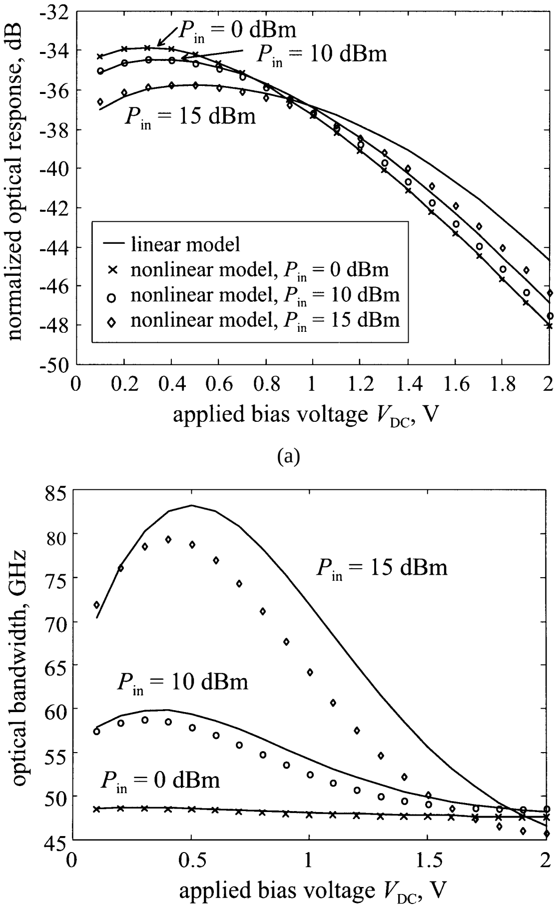

(a)

(b)

Fig. 8. Normalized optical response at: (a) 1 GHz and (b) 3-dB optical bandwidth as functions of the applied bias at different incident optical power. The optical response is normalized to the input optical power.

junction bias voltage V_j. The junction voltage computed by the nonlinear model is higher, on the average, than the one computed by the linear model. Thus, according to Fig. 7(b), the nonlinear model will predict a lower modulation efficiency with respect to the linear model, as indeed results from the comparison of the computed frequency responses in Fig. 6.

As previously stated, the dependence of the microwave-line parameters on the photocurrent causes these parameters to change with the applied bias. As a result, the frequency response of the TW EAM also changes with the applied bias. The amount of this effect, in terms of both low-frequency response and bandwidth, is shown in Fig. 8 for different optical-power levels.

B. RF and Optical-Power Saturation

Linearity and high optical-power handling are key requirements for EAMs suitable for high-performance analog applications [18], [19]. Thus, from a design standpoint, it is important to have tools able to evaluate the effects of RF and optical-power saturation mechanisms on the modulator behavior and, in particular, to predict harmonics and IMP generation. As examples of the nonlinear model capabilities, a linearity analysis of the modulator has been performed under single-tone excitation, as a function of the modulating voltage, as well as of the incident optical power. A sinusoidal tone at 1 GHz was applied.

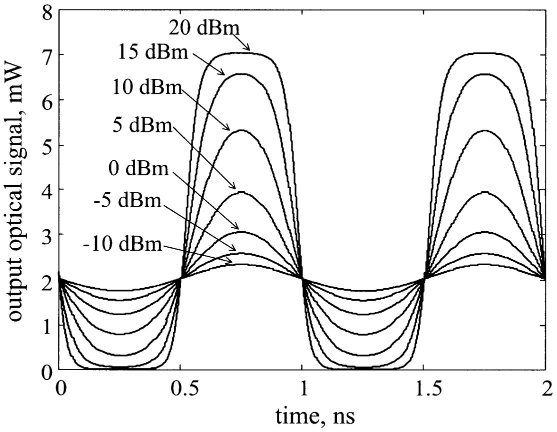

Fig. 9. Time-domain output optical waveforms for different levels of the RF modulating signal.

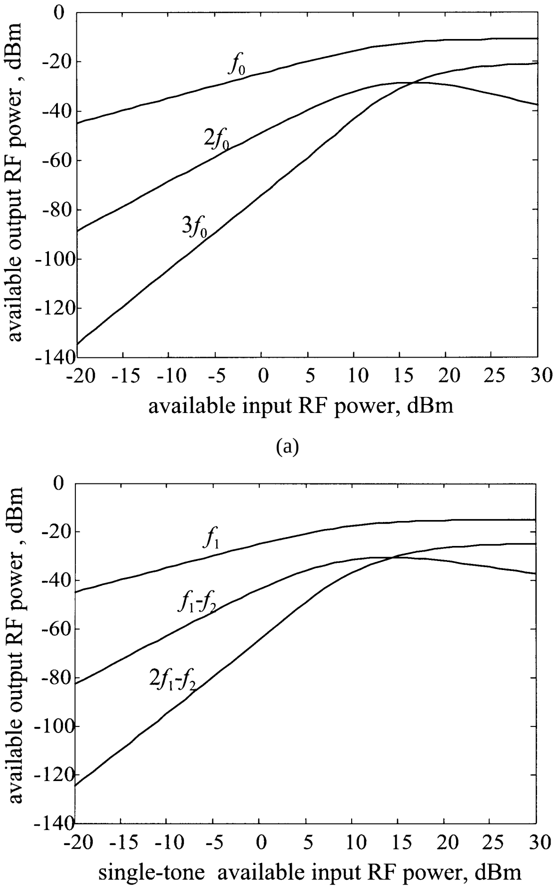

(a)

(b)

Fig. 10. (a) RF harmonics generation and saturation effect under single-tone RF input signal. (b) IMP generation under two-tone RF input signal.

The dc voltage source supplied 0.7-V bias, and the incident optical power was 10 dBm. Fig. 9 shows the time-domain optical waveforms at the output of the modulator for different levels of RF input power. The RF amplitude modulation curve, extracted from the time-domain waveforms, is reported in Fig. 10(a). The receiver responsivity and impedance were set to 0.8 A/W and 50 Ω, respectively. Due to the nonlinear relationship between absorption and voltage, as the modulating signal increases, the optical waveforms deviate from the small-signal sinusoidal be-

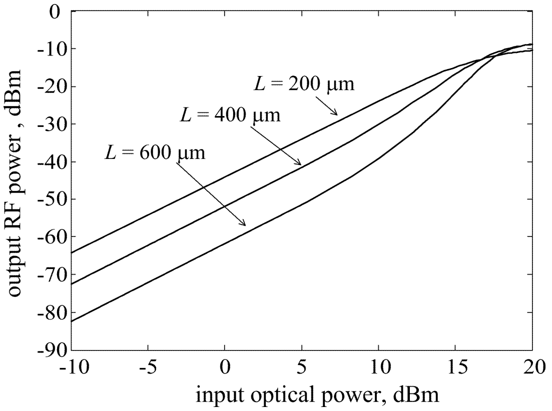

Fig. 11. Optical-power-induced saturation for different device lengths.

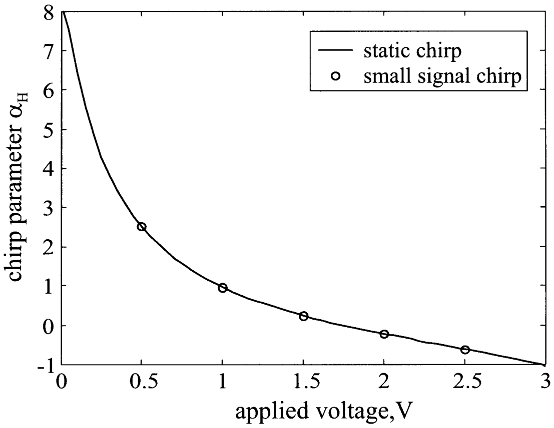

Fig. 12. Dependence of the chirp parameter α_H on the applied voltage for the optical parameters shown in Fig. 5.

havior, yielding saturation of the fundamental signal and harmonics generation, as shown in Fig. 10(a). Finally Fig. 10(b) reports the results of a two-tone simulation at input frequencies of 1 and 1.1 GHz, showing generation of second- and third-order IMPs. By fitting the fundamental and harmonics at low RF input powers, an accurate small-signal multifrequency model can be extracted to be used in system-level simulations.

As for the power saturation, we have compared the behavior of different length TW EAMs with the same active layer. Going to higher lengths is attractive either to decrease the modulator switching voltage or to increase the power-handling capability. However, microwave losses limit the available lengths to a few hundreds micrometers. We have considered three TW EAMs with a length of 200, 400, and 600 μm, corresponding to switching voltage, for 20-dB contrast ratio, of 2.1, 1.26, and 0.96 V, respectively. The dynamic simulation was performed under a sinusoidal tone at 1 GHz, with RF input available power of 0 dBm so that, at low optical power, the modulators operate linearly. The supplied bias voltage was 0.7 V. The results reported in Fig. 11 suggest the following remarks. At low input optical power, the higher the modulator length, the lower the available RF output power is because of the increased optical residual loss $(\alpha_0 L)$. From a design standpoint, a tradeoff can be sought since the higher optical residual loss could cancel the advantage of increased length in terms of reduced V_π. Obviously, the slope of the curves in logarithmic scale is 2 since the RF power is proportional to the square of the optical power. However, as the optical power increases, the slope of the curves corresponding to the 400- and 600-μm EAMs increases. In fact, as previously highlighted, the optical power traveling along the optical waveguide causes "self-biasing" of the device, which leads to a locally varying modulation efficiency (in terms of $k_\alpha = \partial\alpha/\partial V_\mathrm{j}$). Depending on the values of bias voltage and the optical-power level, the local junction voltage can move toward higher values of k_α, resulting in a larger overall modulation efficiency than in the low-power case. This is the case in Fig. 11. Finally, a larger optical saturation power can be observed in longer modulators.

C. Large-Signal Simulations: Frequency Chirp

As is well known, light chirping is a parasitic property of intensity modulated light due to the interdependence between the real and imaginary parts of the refractive index (Kramers–Krönig relationships). Thus, when the optical field is intensity modulated, it also suffers a spurious phase modulation, yielding an instantaneous frequency shift of the optical field. From a system standpoint, frequency chirp limits the available transmission bandwidth in single-mode fiber systems, due to the chromatic dispersion of optical fibers. Thus, evaluation of the modulator chirp is a key task, especially for high-speed long-haul applications.

In small-signal conditions, it is customary to define the chirp parameter α_H, which relates the instantaneous variation of the optical field intensity (P_op) and phase (ϕ) as follows [20]:

$$\frac{d\varphi}{dt} = \frac{\alpha_\mathrm{H}}{2P_\mathrm{op}}\frac{dP_\mathrm{op}}{dt}. \tag{30}$$

The derivative of the phase with time on the left-hand side of (30) represents the instantaneous frequency shift of the output light. For EAMs, α_H can be directly computed from the optical properties of the active material as a function of the applied bias [20]. The resulting α_H is reported in Fig. 12, denoted as "static chirp." For the case under study, α_H greatly varies with the applied bias: it takes values from 8 to -1 when the bias changes from 0 to 3 V. This figure also shows the results obtained from the numerical simulation under small-signal conditions at different bias voltages.

Under large-signal operation, the relationship in (30) is no longer applicable, although the knowledge of the static chirp can provide some qualitative indication. In this case, the frequency chirp of the output optical power must be directly evaluated from the instantaneous optical phase, i.e., $\omega(t) = d\varphi/dt$. Fig. 13 reports the results of a large-signal simulation carried out under different bias conditions. The incident optical power was 10 dBm and the modulating frequency was 10 GHz. At supplied dc voltages of 1 and 1.5 V, the chirp results positive, according to the small-signal prediction, with positive frequency shift on the leading edge of the optical intensity, and negative frequency shift on the trailing edge. As the dc bias is increased to 2 and 2.5 V, negative chirp occurs, reversing the positions of the frequency components, i.e., higher frequency components on the trailing edge and lower frequency components on the leading edge.

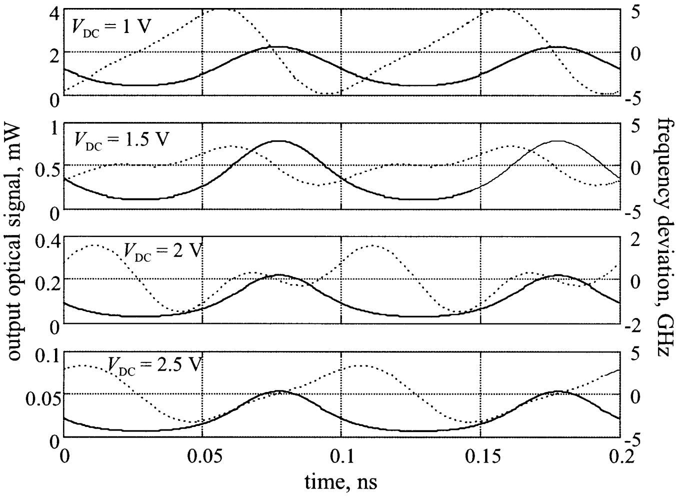

Fig. 13. Time-resolved frequency chirp in large-signal operation at different bias voltage. Solid lines: optical intensity; dashed lines: frequency shift.

IV. CONCLUSION

We have presented a self-consistent time-domain model for the analysis of TW EAMs. The model fully accounts for the nonlinear interaction between the microwave and optical traveling fields. The effects on the bandwidth and modulation efficiency of the nonuniform optical field distribution along the device have been highlighted. A few examples of application have been presented, showing the model to be an efficient tool for the analysis, design, and optimization of TW EAMs intended for analog, as well as digital applications.

ACKNOWLEDGMENT

The authors would like to thank Prof. M. C. Wu and S. Mathai, both of the University of California at Los Angeles (UCLA), for useful discussions on EAM modeling and related system evaluation.

REFERENCES

[1] S. Z. Zhang, Y. J. Chiu, P. Abraham, and J. E. Bowers, "25 GHz polarization insensitive electroabsorption modulators with travelling-wave electrodes," *IEEE Photon. Technol. Lett.*, vol. 11, pp. 191–193, Feb. 1999.

[2] K. Kawano, K. Kohtoku, M. Ueki, T. Itoh, S. Kondoh, Y. Noguchi, and Y. Hasumi, "Polarization insensitive traveling wave electrode electroabsorption (TW-EA) modulator with bandwidth over 50 GHz and driving voltage less than 2 V," *Electron. Lett.*, vol. 33, no. 18, pp. 1580–1581, 1997.

[3] G. L. Li, C. K. Sun, S. A. Pappert, W. X. Chen, and P. K. L. Yu, "Ultrahigh-speed traveling-wave electroabsorption modulator-design and analysis," *IEEE Trans. Microwave Theory Tech.*, vol. 47, pp. 1177–1183, July 1999.

[4] S. Irmscher, R. Lewen, and U. Eriksson, "Microwave properties of ultrahigh-speed traveling-wave electro-absorption modulators for 1.55 ţm," in *Integrated Photonic Research Technical Dig.*, Monterey, CA, June 2001, Paper IME2-1.

[5] Y. J. Chiu, V. Kaman, S. Z. Zhang, and J. E. Bowers, "Distributed effects model for cascaded traveling-wave electroabsorption modulator," *IEEE Photon. Technol. Lett.*, vol. 13, pp. 791–793, Aug. 2001.

[6] B.-S. Kim, Y. Chung, and S.-H. Kim, "Dynamic analysis of widely tunable laser diodes integrated with sampled- and chirped-grating distributed Bragg reflectors and an electroabsorption modulator," *IEICE Trans. Electron.*, vol. E81-C, no. 8, pp. 1342–1349, 1998.

[7] A. Hsu, S.-L. Chuang, W. Fang, L. Adams, G. Nykolak, and T. Tanbun-Ek, "A wavelength-tunable curved waveguide DFB laser with an integrated modulator," *IEEE J. Quantum Electron.*, vol. 35, pp. 961–969, Nov./Dec. 1999.

[8] Y. Kim, H. Lee, J. Lee, J. Han, T. W. Oh, and J. Jeong, "Chirp characteristics of 10-Gb/s electroabsorption modulator integrated DFB lasers," *IEEE J. Quantum Electron.*, vol. 36, pp. 900–908, Aug. 2000.

[9] L. M. Zhang and J. E. Carroll, "Semiconductor 1.55 μm laser source with gigabit/second integrated electroabsorptive modulator," *IEEE J. Quantum Electron.*, vol. 30, pp. 2573–2577, Nov. 1994.

[10] M. Aoki, S. Takashima, Y. Fujiwara, and S. Aoki, "New transmission simulation of EA-modulator integrated DFB-lasers considering the facet reflection-induced chirp," *IEEE Photon. Technol. Lett.*, vol. 9, pp. 380–382, Mar. 1997.

[11] G. P. Agrawal, *Non Linear Fiber Optics*. New York: Academic, 1995.

[12] A. Taflove, *Computational Electrodynamics: The Finite-Difference Time-Domain Method*. Norwood, MA: Artech House, 1995.

[13] A. V. Oppenheim and R. W. Schafer, *Discrete-Time Signal Processing*. Englewood Cliffs, NJ: Prentice-Hall, 1989.

[14] B. Kim, Y. Chung, and J. Lee, "An efficient split-step time-domain dynamic modeling of DFB/DBR laser diodes," *IEEE J. Quantum Electron.*, vol. 36, pp. 787–794, July 2000.

[15] H. Jiang and P. K. L. Yu, "Equivalent circuit analysis of harmonic distortions in photodiode," *IEEE Photon. Technol. Lett.*, vol. 10, pp. 1608–1610, Nov. 1998.

[16] F. Fiedler and A. Schlachetzki, "Optical parameters of InP-based waveguides," *Solid State Electron.*, vol. 30, no. 1, pp. 73–83, 1987.

[17] A. Alping, R. Tell, and S. T. Eng, "Photodetection properties of semiconductor lasers diode detectors," *J. Lightwave Technol.*, vol. LT-4, pp. 1662–1668, Nov. 1986.

[18] G. L. Li, S. A. Pappert, P. Mages, C. K. Sun, W. S. C. Chang, and P. K. L. Yu, "High-saturation high-speed traveling-wave InGaAsP-InP electroabsorption modulator," *IEEE Photon. Technol. Lett.*, vol. 13, pp. 1076–1078, Oct. 2001.

[19] K. K. Loi, J. H. Hodiak, X. B. Mei, C. W. Tu, W. S. C. Chang, D. T. Nichols, L. J. Lembo, and J. C. Brock, "Low-loss 1.3-mm MQW electroabsorption modulators for high-linearity analog optical links," *IEEE Photon. Technol. Lett.*, vol. 10, pp. 1572–1574, Nov. 1998.

[20] F. Koyama and K. Iga, "Frequency chirping in external modulators," *J. Lightwave Technol.*, vol. 6, pp. 87–87, Jan. 1988.

Federica Cappelluti (S'02–M'03) was born in Ortona, Italy, in 1973. She received the Laurea degree in electronic engineering and Ph.D. degree in electronic and communications engineering from the Politecnico di Torino, Turin, Italy, in 1998 and 2002, respectively.

She is currently a Research Assistant with the Dipartimento di Elettronica, Politecnico di Torino. Her research interests concern the modeling and simulation of modulators and photodiodes for RF-on-fiber and high-speed optical communications systems. She is also involved in research on power microwave devices and circuits with an emphasis on electrothermal modeling and stability issues.

Giovanni Ghione (M'87–SM'94) received the Laurea degree in electronics engineering from the Politecnico di Torino, Turin, Italy, in 1981.

From 1983 to 1987, he was a Research Assistant with the Politecnico di Torino. From 1987 to 1990, he was an Associate Professor with the Politecnico di Milano, Milan, Italy. In 1990 he joined the University of Catania, Catania, Italy, as Full Professor of electronics. Since 1991, he has been a Full Professor with the II Faculty of Engineering, Politecnico di Torino. Since 1981, he has been engaged in Italian and European research projects (ESPRIT 255, COSMIC, and MANPOWER) in the field of active and passive microwave computer-aided design (CAD). His current research interests concern the physics-based simulation of active microwave and opto-electronic devices, with particular attention to noise modeling, thermal modeling, and active device optimization. His research interests also include several topics in computational electromagnetics, including coplanar component analysis. He has authored or coauthored over 150 papers and book chapters in the above fields.

Prof. Ghione is member of the Associazione Elettrotecnica Italiana (AEI). He is an Editorial Board member of the IEEE TRANSACTIONS ON MICROWAVE THEORY AND TECHNIQUES.